Publication Year	2020
Acceptance in OA	2025-03-14T12:13:01Z
Title	Characterization of the Ryugu surface by means of the variability of the near-infrared spectral slope in NIRS3 data
Authors	GALIANO, Anna, PALOMBA, Ernesto, D'Amore, M., Zinzi, A., DIRRI, Fabrizio, LONGOBARDO, Andrea, Kitazato, K., Iwata, T., Matsuoka, M., Hiroi, T., Takir, D., Nakamura, T., Abe, M., Ohtake, M., Matsuura, S., Watanabe, S., Yoshikawa, M., Saiki, T., Tanaka, S., Okada, T., Yamamoto, Y., Takei, Y., Shirai, K., Hirata, N., Hirata, N., Matsumoto, K., Tsuda, Y.
Publisher's version (DOI)	10.1016/j.icarus.2020.113959
Handle	http://hdl.handle.net/20.500.12386/36794
Journal	ICARUS
Volume	351

Characterization of the Ryugu surface by means of the variability of the Near-Infrared spectral slope in NIRS3 data

A. Galiano[1], E. Palomba[1,2], M. D'Amore[3], A. Zinzi[2], F. Dirri[1], A. Longobardo[1], K. Kitazato[4], T. Iwata[5], M. Matsuoka[5], T. Hiroi[6], D. Takir[7], T. Nakamura[8], M. Abe[5], M. Ohtake[5], S. Matsuura[9], S. Watanabe[5,10], M. Yoshikawa[5], T. Saiki[5], S. Tanaka[5], T. Okada[5], Y. Yamamoto[5], Y. Takei[5], K. Shirai[5], N. Hirata[11], N. Hirata[4], K. Matsumoto[12], Y. Tsuda[5].

[1]INAF-IAPS, Rome, Italy (anna.galiano@inaf.it), [2]SSDC-ASI, Rome, Italy, [3]German Aerospace Center, Institute of Planetary Research, Berlin, Germany, [4]University of Aizu, Aizu-Wakamatsu 965-8580, Fukushima, Japan, [5]Institute of Space and Astronautical Science (ISAS), Japan Aerospace Exploration Agency, Sagamihara, 252-5210, Japan, [6]Department of Earth, Environmental and Planetary Sciences, Brown University, Providence, RI 02912, USA, [7]Jacobs/NASA Johnson Space Center, USA, [8]Tohoku University, Miyagi, Japan, [9]Kwansei Gakuin University, Hyogo, Japan, [10]Nagoya University, Nagoya 464-8601, [11]Kobe University, Kobe 657-8501, Japan, [12]National Astronomical Observatory of Japan, Mitaka 181-8588, Japan.

Abstract

The Near-Earth Asteroid 162173 Ryugu (1999 JU3) was investigated by the JAXA Hayabusa2 mission from June 2018 to November 2019. The data acquired by NIRS3 spectrometer revealed a dark surface with a positive near-infrared spectral slope. In this work we investigated the spectral slope variations across the Ryugu surface, providing information about physical/chemical properties of the surface.

We analysed the calibrated, thermally and photometrically corrected NIRS3 data, and we evaluated the spectral slope between 1.9 μm and 2.5 μm, whose values extend from 0.11 to 0.28 and the mean value corresponds to 0.163±0.022. Starting from the mean value of slope and moving in step of 1 standard deviation (0.022), we defined 9 "slope families", the Low-Red-Slope families (LR1, LR2 and LR3) and the High-Red-Sloped families (HR1, HR2, HR3, HR4, HR5, HR6). The mean values of some spectral parameters were estimated for each family, such as the reflectance factor at 1.9 μm, the spectral slope, the depth of bands at 2.7 μm and at 2.8 μm. A progressive spectral reddening, darkening and weakening/narrowing of OH bands is observed moving from the LR families to the HR families.

We concluded that the spectral variability observed among families is the result of the thermal metamorphism experienced by Ryugu after the catastrophic disruption of its parent body and space weathering processes that occurred on airless bodies as Ryugu, such as impact cratering and solar wind irradiation. As a consequence, the HR1, LR1, LR2 and LR3 families, corresponding to equatorial ridge and crater rims, are the less altered regions on Ryugu surface, which experienced the minor alteration and OH devolatilization; the HR2, HR3, HR4, HR5 families, coincident with floors and walls of impact craters, are the most altered areas, result of the three processes occurring on Ryugu. The strong reddening of the HR6 family (coincident with Ejima Saxum) is likely due to the fine-sized material covering the large boulder.

1. Introduction

The JAXA Hayabusa2 mission investigated the Near-Earth Asteroid 162173 Ryugu (1999 JU3) from June 2018 to November 2019. By the examination of a primitive asteroid as Ryugu, the aim of mission was to elucidate our knowledge about the formation and evolution of the Solar System, such as: the

conditions that led to the formation of planets from planetoids; the material present in the primordial Solar System and which contributed to the formation of life on Earth.

The Hayabusa2 mission *(Watanabe et al., 2017)* was launched on the 3rd December 2014 and arrived at the Cb-type asteroid Ryugu on the 27th June 2018. The spacecraft allowed to perform remote-sensing analysis from the Home Position (HP, 20 km in altitude) and in-situ operations, in addition to 2 touch-downs procedures.

Remote-sensing analyses were carried out thanks to the laser altimeter Light Detection and Ranging (LIDAR), the Thermal Infrared Camera (TIR), the Optical Navigation Camera (ONC) and the Near-Infrared Spectrometer (NIRS3).

By using a pulse laser with a wavelength of 1064 nm, LIDAR measured the altitude of spacecraft with respect to the Ryugu's surface and was used to measure shape, gravity and surface characteristics of the asteroid. LIDAR also operated as navigation sensor for approach and touch-down operations, since it can measure altitudes from 25 km to 30 m (*Mizuno et al., 2017*). TIR investigated the surface of Ryugu in the 8-12 µm spectral range with a resolution of 20 m/pixel from the HP (*Arai et al., 2017*), whereas the ONC camera acquired images of the surface in the visible range. ONC was equipped with a telescopic camera (T) and two wide-angle cameras (W1 and W2). The telescopic camera acquired images with a spatial resolution of 2 m/pixel (HP) in 7 filters: 390 nm (u), 480 nm (b), 550 nm (v), 589.5 nm (Na), 700 nm (w), 860 nm (x), 950 nm (p) (*Kameda et al., 2017*). NIRS3 is a point spectrometer and acquired reflectance spectra of Ryugu surface in the spectral range included between 1.8 and 3.2 µm. The spectral resolution of NIRS3 is 18 nm and the spatial resolution is 40 m/pixel (HP) (*Iwata et al., 2017*).

During the mission, in-situ analyses were performed by means of the release on the surface of two rovers (MINERVA-II-1A and MINERVA-II-1B) on the 21st September 2018 and the lander MASCOT on the 4th October 2018.

The first touch-down operation was performed on the 21st February 2019 in the L08 site (-5/10 °N; 195/210 °E): surficial grains of Ryugu were successfully collected and stored in the collection

chamber. During the Small Carry-on Impactor (SCI) Operation *(Saiki et al., 2013)*, on the 5th April 2019, an artificial crater was created in the S01 site (5 °N; 303 °E), exposing less altered material from the subsurface. The artificial crater was named as "Omusubi-Kororin crater". The second touch-down operation occurred on the 11th July 2019 in the S01 and grains in proximity of Omusubi-Kororin crater were collected. With high probability, grains of subsurface material exposed because of crater formation were collected. The spacecraft departed from Ryugu on the 13th November 2019 and will reach the Earth for the end of 2020: the collected grains will be released to Earth by means of a re-entry capsule *(Tachibana et al., 2017)* and will be analysed in terrestrial laboratories.

The Near-Earth asteroid Ryugu has a semi-major axis of 1.19 au, a perihelion and an aphelion distance of 0.96 au and 1.42 au, respectively, belonging to the Apollo group. Ryugu has a revolution period of 1.297 yr and a rotation period of 7.63 h. The daytime surface temperature of Ryugu ranges from 330 K to 370 K when the asteroid is at the heliocentric distance of 1.01 au *(Kitazato et al., 2019).*

Images acquired by ONC revealed a dark top-shaped asteroid, e.g with a round shape and an equatorial ridge. The equatorial radius is about 502 ± 2 m, and the surface is covered by boulders and impact craters.

The average reflectance factor of Ryugu's surface, derived at the standard laboratory observation angles, i.e. incidence angle 30°, emission angle 0° and phase angle 30°, is (1.88 ± 0.17) % at 0.55 μm, darker than any other meteorites *(Sugita et al., 2019)*, and the geometric albedo is (4.5 ± 0.2) % at 0.55 μm *(Watanabe et al., 2019).* The bulk density is 1.19 ± 0.02 g/cm^3, suggesting that Ryugu is a rubble pile object likely formed from reaccumulation of fragments generated by a catastrophic disruption of its parent body *(Michael et al., 2001; Watanabe et al., 2019)*. The equatorial ridge of Ryugu shows some geological features, such as: large unaltered craters overlying it, suggesting that equatorial craters formed after the ridge; imbricated boulders, indicating a mass wasting from the equator to midlatitudes *(Watanabe et al., 2019).* Ryugu is thought to be migrated in its current Near-Earth orbit from the Main Belt, likely through the ν_6 resonance *(Tardivel et al., 2018; Bottke et al., 2015).* Since the collision frequency is higher in the Main Belt than in near-Earth orbit, it is likely

that craters with diameter greater than 100 m formed when Ryugu was in the Main Belt *(Sugita et al., 2019)*. In particular, larger craters could be formed in the Main Belt and they could reflect the resurfacing processes occurred at such heliocentric distances, whereas smaller craters of about 30 m are instead suggested to be formed in the Near-Earth orbit, whose permanence started at least 8 Myr ago *(Takaki et al., 2019).*

The spectral slope estimated in the visible range, i.e from 0.48 μm to 0.86 μm is bluer (negative) at poles and equatorial ridge: they are topographic highs subjected to gradual erosion, which could lead to the exposure of fresher surface material *(Sugita et al., 2019)* through mass wasting from the equator and polar region to midlatitudes. Crater floors show redder spectral slope (positive slope) and darkening, suggesting that such spectral modifications occur when the Ryugu material is exposed to the space *(Sugita et al., 2019)*. The cause of the VIS spectral reddening and darkening is not certain and could be due to space weathering or to other processes such as coating of redder and darker dust *(Sugita et al., 2019).*

Furthermore, a west/east dichotomy was observed: the western side (160°E-70°W) shows a lower number density of large craters and therefore a smoother surface than the eastern side, explained as the occurrence of smaller grain size of regolith in the western hemisphere *(Sugita et al., 2019)*. Models simulating the formation of the Ryugu's top shape suggested that the western region could be the result of a structural relaxation occurred when the spin rotation of Ryugu was, in the past, faster than the actual one. Deformation at a fast spin can occur globally in a short time scale, explaining the perfect circularity of the Ryugu's equatorial ridge as a uniform distribution of fluidized material *(Hirabayashi et al. 2019)*.

Reflectance spectra acquired by NIRS3 spectrometer show a low reflectance factor coincident with ONC results: the global averaged reflectance at 2.0 μm (corrected to a standard viewing geometry with incidence angle of 30°, emergence angle of 0° and phase angle of 30°) is (1.7±0.2)% *(Kitazato et al., 2019).* However, some brighter areas have been identified on the equatorial ridge, crater rims and individual boulders *(Kitazato et al., 2019)*. Spectra are red-sloped in the 2.0-2.5 μm spectral range

and a weak and narrow absorption band at about 2.72 μm is present everywhere *(Kitazato et al., 2019)*. The 2.72-μm feature was related to hydroxyl (OH) symmetric stretching in Mg-rich phyllosilicates (such as serpentine and saponite) and the low reflectance value could be explained with high abundances of carbon, opaque minerals (such as magnetite) or products of shock-induced metamorphism (dark glassy component). By comparing NIRS3 spectra of Ryugu with spectra of meteorites, a similarity with carbonaceous chondrites (CCs) meteorites emerged, in particular CI and CM carbonaceous chondrites, i.e. primitive material containing organic compounds and water-bearing minerals *(Cloutis et al., 2011 and references therein)*. The spectrum of Ryugu seems to be like thermally metamorphosed CI chondrites (such as the spectrum of CI Ivuna meteorite heated at 500 °C) or shocked CM chondrites (such as the spectrum of the CM2 shocked MET01072 meteorite). Such results suggest that Ryugu experienced a thermal metamorphism, likely as a consequence of the collisional event that fragmented the parent body and that allowed to form as reaccumulation of fragments *(Watanabe et al., 2019)*: the shock and post-shock event could have caused the darkening of the surface and the dehydration and dehydroxylation of hydrated minerals *(Kitazato et al., 2019)*. However, Ryugu is a body with no atmosphere or magnetic field, therefore it is constantly subjected to space weathering effects such as solar wind irradiation and micro-meteoritic impacts, which can alter the spectral properties of the surface *(Kitazato et al., 2019)*.

In this work we investigated the variations in spectral slope across the surface of Ryugu, which could provide information about physical/chemical properties of the surface.

The NIRS3 dataset is described in *Section 2*, whereas the tools used for the analysis are explained in *Section 3*. In *Section 4* the method applied to define the slope families is illustrated and *Section 5* involves the spectral analysis performed. The distribution of slope families on Ryugu surface is shown in *Section 6*, whereas *Section 7* includes the discussion of results and conclusions are presented in *Section 8*.

2. NIRS3 dataset

153 The NIRS3 point spectrometer started to acquire reflectance spectra of Ryugu surface on the 21st June
154 2018 from a distance of 70 km. On 27th June, the spacecraft was set at an altitude of 20 km from the
155 Ryugu's surface (HP). On 11th and 19th July 2018, NIRS3 operated in scanning mode, i.e, the slews
156 of spacecraft were combined with the rotation of the asteroid, to obtain near-global spectral
157 observations. On 6th to 7th August, the spacecraft performed a descent close to the surface down to 1
158 km (gravity measurements) and acquired spectral data of 2 m/pixel in spatial resolution. Then,
159 throughout the Hayabusa2 operations (such as the release of rovers and landers, touch-down
160 operations), NIRS3 acquired the spectral data with a higher spatial resolution (about 1 m/pixel).

161 In this work we analyse the NIRS3 data acquired on 11th July 2018 (when the spacecraft was at HP)
162 and on 19th July 2018 (when the spacecraft was at an altitude of 13 km), since a global coverage of
163 the Ryugu surface was obtained with these observations. Then, we also used data acquired on the 10th
164 July 2018 (HP), focused in the proximity of the equatorial ridge. The selected data are calibrated,
165 thermally and photometrically corrected *(Kitazato et al., 2019)*, in order to avoid, in our analysis, the
166 occurrence of spectral variations due to observation viewing and thermal contribution, even if some
167 thermal residuals could still affect the spectra *(Kitazato et al., 2019)*. Data acquired on 10th and 11th
168 July 2018 are characterized by a spatial resolution of 35 m/pixel and data obtained on 19th July have
169 a spatial resolution of 23 m/pixel.

170

171 ## 3. Tools

172 We spectrally analysed the NIRS3 data by estimating and comparing some useful spectral parameters.
173 NIRS3 spectra show an absorption band at 2.72 μm, related to Mg-rich pyllosilicates *(Kitazato et al.,*
174 *2019)*. However, a secondary absorption band at 2.8 μm is also present, as can be observed in ***Figure***
175 ***1***, where the averaged spectrum of Ryugu is shown.
176 The spectral range considered in this work is included between 1.8 and 3.0 μm: we decided to cut the
177 reflectance spectra since the spectral region between 3.0 μm and 3.2 μm is affected by calibration

178 residuals *(Kitazato et al., 2019).* We applied a smoothing procedure on reflectance spectra by
179 replacing the reflectance at each NIRS3 spectral band with the average of reflectance among the three
180 closest NIRS3 spectral bands. The procedure was applied to reduce oscillation in the signal (that for
181 dark objects as Ryugu is due to low signal-to-noise ratio) which could alter the estimation of spectral
182 parameters, as previously investigated for Ceres *(Galiano et al., 2018).*
183 The spectral parameters taken into account in the analysis are spectral slope, reflectance factor at 1.9
184 μm ($R_{1.9}$), Band Center (BC) and Band Depth (BD) of absorption bands. These spectral indices are
185 usually used both in laboratory spectra and in remotely sense spectral data sets to detect the
186 mineralogical composition of a planetary surface and the physical properties of the surface regolith
187 *(Clark and Roush, 1984)*. The spectral slope can suggest chemical variations in composition, physical
188 properties of regolith such as differences in the granulometry, as well as clues about space weathering
189 effects; the band center can be indicative of the mineral's specie responsible of the spectral features;
190 the band depth can provide a qualitative information about the abundance of minerals. The band depth
191 value can depend of grain size distribution *(Adams, 1974; Clark, 1999)* and is also indicative of the
192 occurrence of dark component, which tend to reduce or even suppress the absorption bands of
193 diagnostic minerals.
194 The spectral slope was estimated in the spectral range between 1.9 and 2.5 μm (represented by a red
195 line ***in Figure 1***), by using the expression:

196 $$Spectral\ slope = \frac{R_{2.5}-R_{1.9}}{\lambda_{2.5}-\lambda_{1.9}} \cdot \frac{1}{R_{1.9}},$$

197 where $\lambda_{2.5}$ and $\lambda_{1.9}$ are the wavelengths at 2.5 μm and 1.9 μm, respectively and $R_{2.5}$ and $R_{1.9}$ are the
198 corresponding reflectance values.
199 To estimate BC and BD, the spectral features were isolated by removing the spectral continuum, fitted
200 by a straight line whose endpoints are located on the bands' shoulders, following the method
201 described in *Galiano et al. (2018)*. In particular, to estimate the BC of 2.7 and 2.8 μm absorption
202 band, a unique continuum for the two bands was produced (blue line in ***Figure 1***): the left shoulder

was estimated as the maximum reflectance value between 2.5 and 2.65 µm and the right shoulder as the maximum reflectance value between 2.85 and 2.95 µm. The band center for the 2.7 µm band was forced to be detected between 2.7 and 2.75 µm, whereas the band center for the 2.8 µm band was detected in the 2.8-2.85 µm range.

The band center is the wavelength corresponding to the minimum reflectance value in the isolated absorption band (***Figure 2***), whereas the band depth is obtained as $1 - \frac{R_{bc}}{R_c}$, where R_{bc} is the reflectance at the band center and R_c is the reflectance at the continuum *(Clark and Roush, 1984)*.

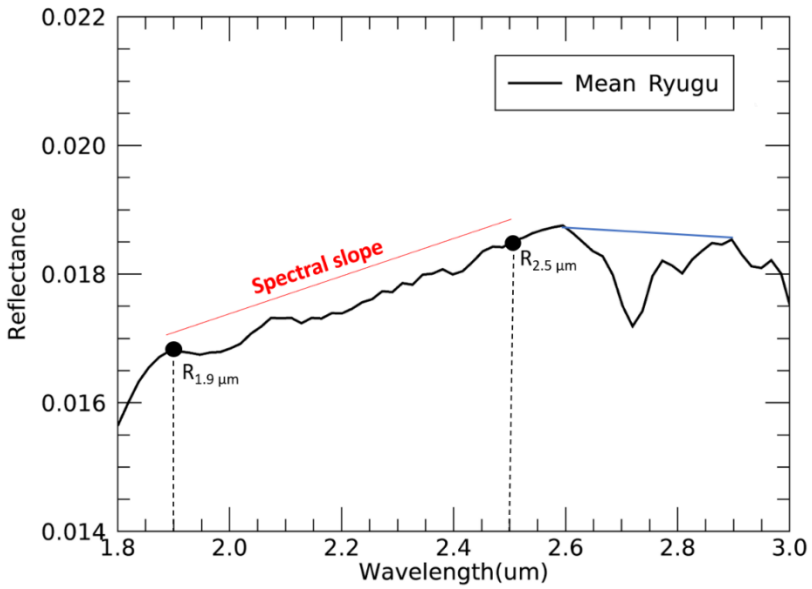

Figure 1: Mean spectrum of Ryugu surface, where the spectral slope (red line), spectral continuum for 2.7 and 2.8 µm bands (blue line) and reflectance factor at 1.9 µm ($R_{1.9}$) and at 2.5 µm ($R_{2.5}$) are represented.

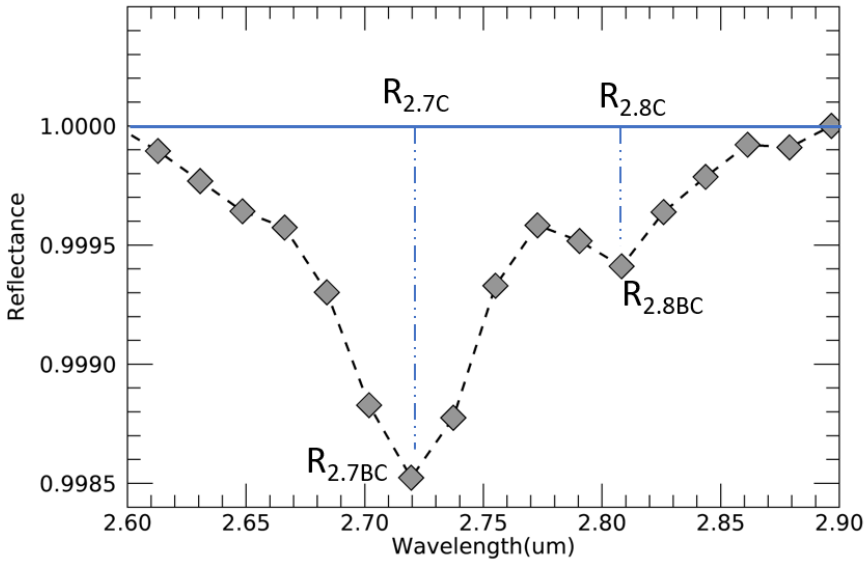

Figure 2: The 2.7-µm and 2.8-µm isolated bands, after the removal of the unique continuum (represented by the blue line). The NIRS3 spectral bands are the grey diamonds and values of reflectance useful for the estimation of band depths are marked.

To search for correlations between spectral parameters, we used the Pearson correlation coefficient (PCC) *(Palomba et al., 2015; Longobardo et al., 2019a)*. PCC estimates a linear correlation between two variables, X and Y, by measuring the covariance of variables (cov(X,Y)) and their standard deviations (σ_X and σ_Y). PCC is defined as $\frac{cov(X,Y)}{\sigma_X \cdot \sigma_Y}$ with the resulting value included between -1 (suggesting an anti-correlation) and 1 (correlation). If the Pearson value is included between 0 and 0.3, the correlation is weak; for values between 0.3 and 0.7 the correlation is moderate; a strong correlation is obtained for values greater than 0.7. A Pearson coefficient close to 0 suggests the absence of any link between parameters.

In this work, we estimated the PCC by using a meticulous approach previously applied in *Galiano et al. (2019)*: we calculated the PCC thousand times, by selecting, each times, random values of X and Y included, respectively in the X-σ_X and X+σ_X range and in the Y-σ_Y and Y+σ_Y range. Then, by

taking into account the thousands of values of PCC so estimated, we obtained the mean value and standard deviation of PCC.

We investigated the presence of possible thermal residuals in reflectance spectra by relating, for each data, the reflectance at 3.0 μm and at 1.9 μm as a function of temperature. We selected these specific wavelengths since they are, respectively, inside and outside the thermal emission region *(Kitazato et al., 2019)*. For each temperature bin (width of 1 K) we estimated the mean values of both reflectance at 3.0 μm and at 1.9 μm. The 3.0 μm shows a slight dependence with temperature, differently than the 1.9 μm, that is highlighted by performing their ratio. The percentage variation in the ratio is about 3% that corresponds to 0.001 in reflectance, that is comparable with the reflectance uncertainty due to radiometric calibration *(Kitazato et al., 2019)*.

Furthermore, the error introduced by the thermal removal was estimated by following the method yet used in *Tosi et al. (2018)*. For each pixel, we estimated the standard deviation of reflectance value at the wavelength of 3.0 μm and at 1.9 μm, respectively inside and outside the thermal emission region *(Kitazato et al., 2019).* The standard deviation of the reflectance value at 3.0 μm is 0.008, as well as the standard deviation of the reflectance value at 1.9 μm.

These two methods allow us to conclude that the uncertainties introduced by the thermal emission removal are negligible and we are confident that the spectral parameters estimated and used for the analysis are not affected by thermal residuals.

4. Definition of slope families

The slope for each NIRS3 spectrum was estimated in the spectral range between 1.9 and 2.5 μm, whose values range from 0.11 to 0.28; the mean value of slope (MS, i.e. Mean Slope) corresponds to 0.163 and the standard deviation (σ) is 0.022.

The map of spectral slope, superposed on Ryugu shape model, is shown in ***Figure 3***. Globally, the positive spectral slope characterizes the Ryugu surface, even if a higher reddening occurs in localized areas such as crater floors and saxa.

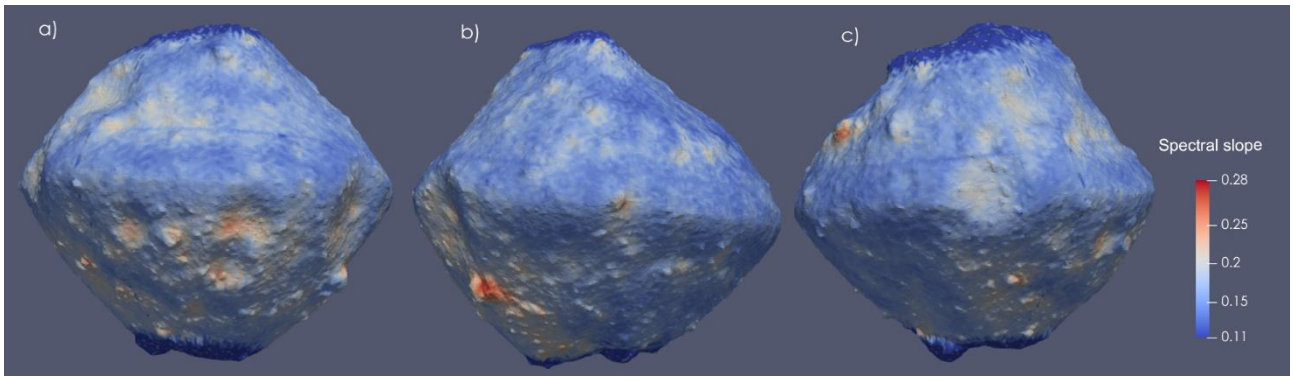

Figure 3: Map of spectral slope of Ryugu superposed on the shape model for longitude range 0-120°E (*Image a*); longitude range 120-240°E (*Image b*); longitude range 240-360°E (*Image c*).

Statistical analysis of spectral parameters has been demonstrated as a useful tool to study surface properties of asteroids *(e.g., Longobardo et al., 2014; 2019b)*. We performed a statistical analysis of spectral slope to investigate the Ryugu surface, by defining different slope "families".

Starting from the mean value of slope and moving in steps coincident with 1σ, we obtained 9 families (***Table 1***). All families are characterized by positive spectral slope, but we identified as "High-Red-sloped families (HR)" the areas with a more positive spectral slope than MS and as "Low-Red-sloped families (LR)" the regions characterized by a lower spectral slope than MS.

A total of 3 "LR" families and 6 "HR" families were detected. The HR1 family includes areas with spectral slope values between MS and MS+1σ; the HR2 involves regions with spectral slope values included between MS+1σ and MS+2σ and so on. Similarly, the LR1 family contains areas with a slope between MS-1σ and MS, the LR2 includes areas with slope ranging from MS-2σ and MS-1σ, and so on.

In ***Figure 4***, the frequency of spectral slope values is shown. The greatest number of spectra (9898 spectra) belongs to the LR1 family, suggesting that the 40.7% of the Ryugu surface exhibits a spectral slope included between 0.141 and 0.163. The LR3 family includes 109 spectra, therefore the 0.45%

of the Ryugu surface reveales the flattest spectral slope, with values in the 0.103-0.119 range. The 10 reflectance spectra with the reddest slope (corresponding to the 0.04% of the Ryugu surface) belongs to the HR6 family and the highest value reaches 0.29.

Table 1: List of the slope families defined in this work. Each column describes for each family: the name of the slope family; the range in terms of standard deviation; the minimum and maximum value of spectral slope included in the family; the number of thermally corrected spectra in the family and the relative percentage.

Family	**Range**	**Min Value of Spectral Slope**	**Max Value of Spectral Slope**	**Number of spectra**	**Percentage of spectra**
LR3	MS-3σ/MS-2σ	0.103	0.119	109	0.45%
LR2	MS-2σ/MS-1σ	0.119	0.141	3550	14.6%
LR1	MS-1σ/MS	0.141	0.163	9898	40.7%
HR1	MS/MS+1σ	0.163	0.184	6964	28.6%
HR2	MS+1σ/MS+2σ	0.184	0.206	2885	11.9%
HR3	MS+2σ/MS+3σ	0.206	0.227	733	3.0%
HR4	MS+3σ/MS+4σ	0.228	0.249	127	0.52%
HR5	MS+4σ/MS+5σ	0.250	0.271	36	0.15%
HR6	MS+5σ/MS+6σ	0.273	0.290	10	0.04%

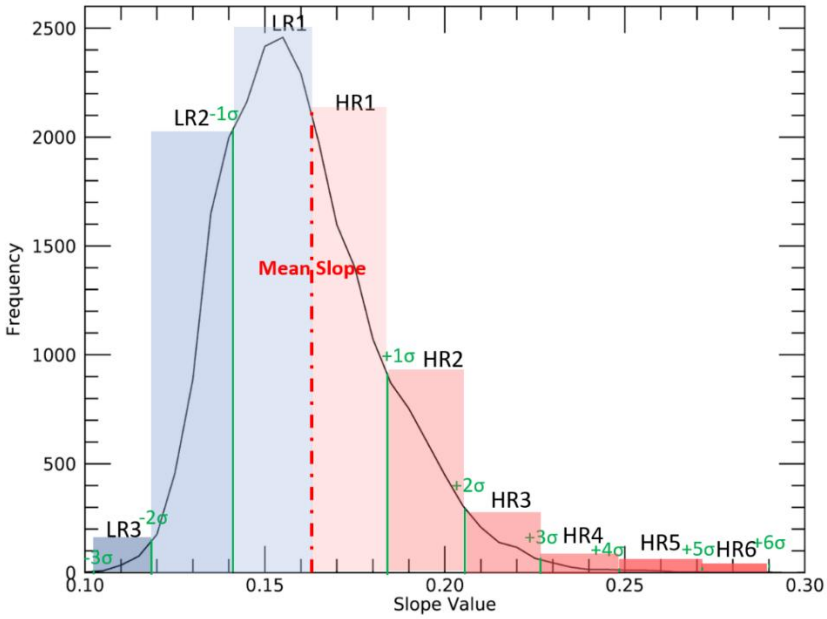

Figure 4: Frequency plot of spectral slope (black gaussian curve), where the mean value of slope (0.163) is indicated with a red dash-dotted line. Each slope family is included in rectangle, where the short side is obtained with the range of spectral values for the considered family and the long sides is defined with the frequency of slope values. The LR families are contained in blue rectangles and HR families are in red rectangles. The range in term of standard deviation is expressed in green color.

The mean spectra of LR families (***Figure 5***) and the mean spectra of HR families (***Figure 6***) show the occurrence of the absorption band at 2.72 µm and at 2.8 µm, as observed on the mean spectrum of Ryugu, which is shown for comparison both in ***Figure 5*** and in ***Figure 6***.

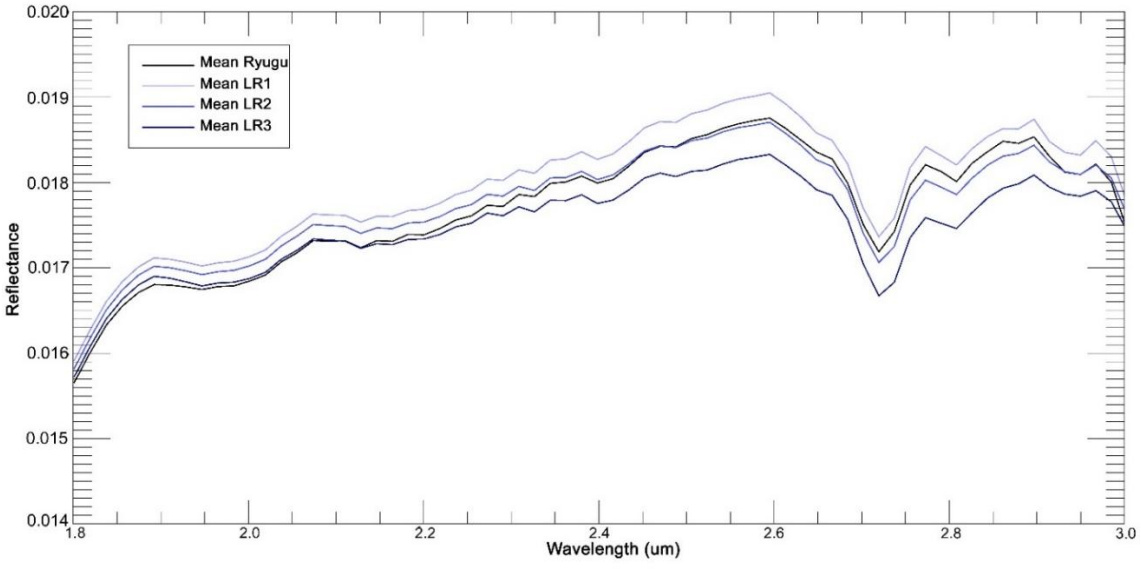

Figure 5: Mean spectra of LR families (blue spectra) compared with the mean spectrum of Ryugu surface (black spectrum).

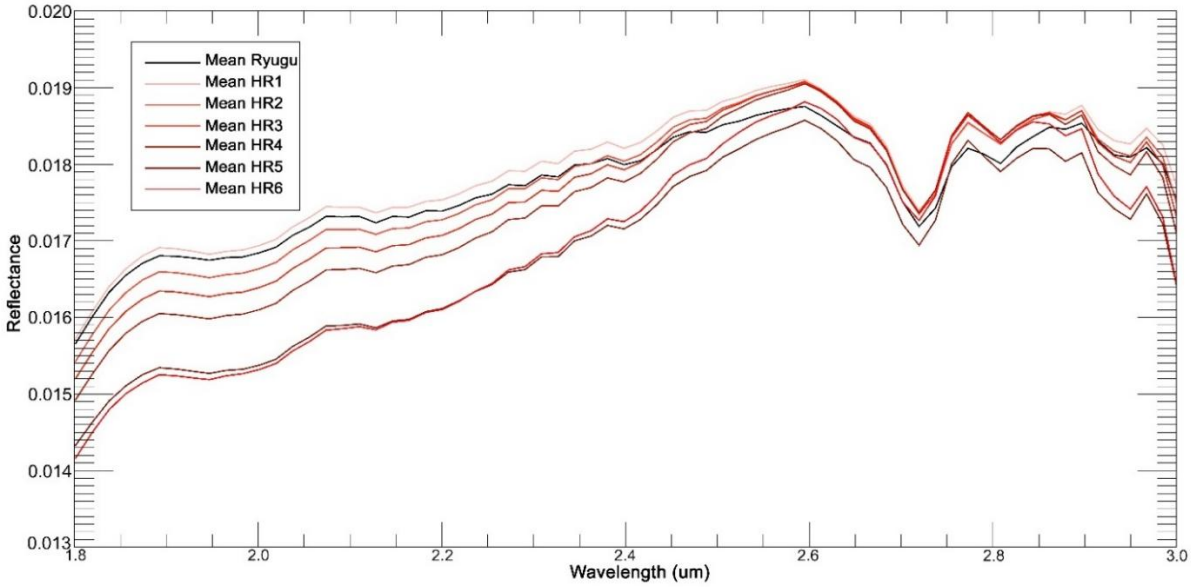

Figure 6: Mean spectra of HR families (red spectra) compared with the mean spectrum of Ryugu surface (black spectrum).

For each family, we estimated mean values and standard deviations of the spectral slope, reflectance factor at 1.9 µm ($R_{1.9}$), Band Center (BC) and Band Depth (BD) of absorption bands at 2.72 µm and 2.8 µm. No variation in the 2.7BC and 2.8BC occurs among the 9 slope families: the 2.7BC is located at 2.72 µm and the 2.8BC is at 2.81 µm for all the families. This result suggests that the minerals responsible of the 2.7 and 2.8 µm absorption bands are the same across the Ryugu surface. The other spectral parameters estimated, and the corresponding standard deviation (σ) are reported, for each family, in ***Table 2***.

Table 2: List of spectral parameters estimated. For each family of slope, the columns represent the mean values and standard deviations for: 2.7BD, 2.8BD, reflectance factor at 1.9 µm ($R_{1.9}$), spectral slope estimated between 1.9 and 2.5 µm.

Family	2.7BD	$\sigma_{2.7BD}$	2.8BD	$\sigma_{2.8BD}$	$R_{1.9}$	$\sigma_{R_{1.9}}$	SLOPE	σ_{SLOPE}
LR3	0.0857	0.0049	0.0397	0.0058	0.0169	0.0004	0.1147	0.0035
LR2	0.0825	0.0044	0.0361	0.0051	0.0170	0.0004	0.1345	0.0049

LR1	0.0825	0.0047	0.0336	0.0054	0.0171	0.0005	0.1522	0.0062
HR1	0.0829	0.005	0.0318	0.0056	0.0169	0.0005	0.1720	0.0061
HR2	0.0830	0.0049	0.0295	0.0059	0.0166	0.0005	0.1935	0.0060
HR3	0.0824	0.0051	0.0266	0.0058	0.0163	0.0006	0.2141	0.0059
HR4	0.0812	0.0055	0.0247	0.0059	0.0161	0.0007	0.2351	0.0058
HR5	0.0803	0.0067	0.0223	0.0078	0.0153	0.0008	0.2583	0.0058
HR6	0.0778	0.0058	0.0199	0.066	0.0153	0.0009	0.2815	0.0066

5. Spectral analysis of slope families

By relating the $R_{1.9}$ and the spectral slope of the slope families (green diamonds), a strong anti-correlation can be observed (***Figure 7***), with a Pearson coefficient of -0.83±0.02. The LR families show a reflectance variation of about 1%, whereas a strong darkening and reddening occurs in the HR family with increasing spectral slope (showed by the dark line fit linking the HR1 to the HR6 family in ***Figure 7***). For comparison, the spectral slope and reflectance factor for mean Ryugu (red diamond) is also shown in ***Figure 7***, that is almost coincident with the HR1 family. However, the general trend observed is that flatter spectra (with less positive spectral slope) have a higher reflectance value, whereas redder spectra (with a more positive spectral slope) have a lower reflectance value: darker areas on Ryugu surface show a more positive spectral slope.

A strong anti-correlation also emerges between the 2.7BD and the spectral slope of the slope families (***Figure 8***) with a Pearson coefficient of -0.83±0.01. LR3 is the family with flatter spectra and with deeper 2.7BD, whereas the HR6 is the family involving redder spectra and with weaker 2.7 BD. As suggested by the scatterplot, darker areas are less hydroxylated and exhibit spectral reddening, whereas brighter areas are more hydroxylated and show a spectral flattening.

The band depth of 2.7 µm absorption feature was also related to the band depth of 2.8 µm one and a strong correlation among the slope families, with a Pearson value of 0.8±0.01, can be observed in ***Figure 9***. The absorption band related to O-H stretching is located at about 2.8 µm in spectra of some serpentine polymorphs (hydrous magnesium iron phyllosilicates), in particular in the cronstedtite spectra *(Clark et al., 2007)*, a Fe-serpentine. The strong correlation between the two bands could

suggest that they could be both related to the O-H stretching of two types of hydroxyl-bearing minerals.

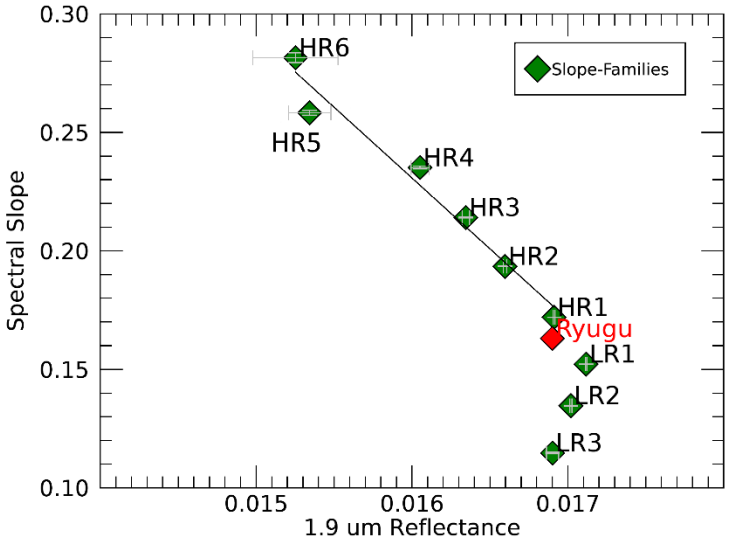

Figure 7: Scatterplot of spectral slope versus reflectance factor at 1.9 µm for the slope families (green diamonds) and mean Ryugu (red diamond). A strong anti-correlation links the two parameters, suggesting that darker areas are characterized by a more positive spectral slope.

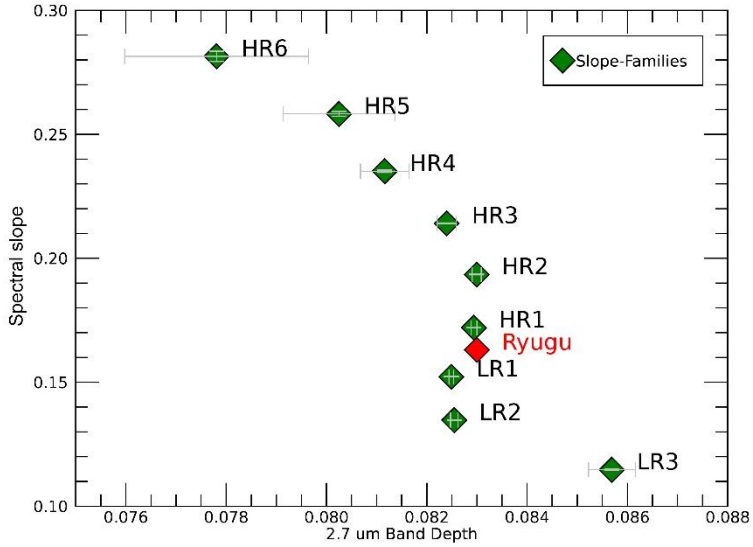

Figure 8: Scatterplot of spectral slope versus band depth at 2.7 µm (2.7BD) for the slope families (green diamonds) and mean Ryugu (red diamond). The anti-correlation between the two parameters suggests that the spectral reddening induces also a weakening in the OH band.

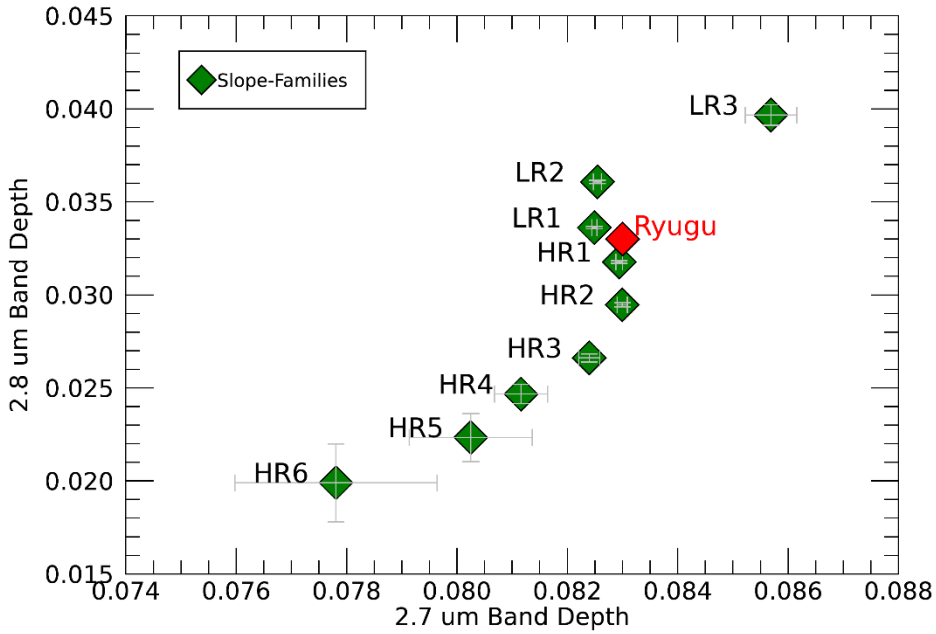

Figure 9: Scatterplot of band depth at 2.7 µm (2.7BD) versus band depth at 2.8 µm (2.8BD) for the slope families (green diamonds) and mean Ryugu (red diamond).

From the spectral analysis of the 9 slope families, the spectral reddening is related to a spectral darkening at 1.9 µm and to a weakening of the 2.7 µm band, as can be easily observed in ***Figure 10***, where the mean spectrum of the HR6 (red spectrum; the family with the reddest spectral slope) and LR3 (blue spectrum; the family with the flattest spectra) families are compared with the spectrum of mean Ryugu (black spectrum). In ***Figure 11***, the isolated and normalized OH bands for the mean spectra of the LR3 and HR6 families are shown, compared with the isolated bands of the mean Ryugu spectrum. As can be noted, the LR3 family (blue spectrum) shows, in addition to deeper 2.7 and 2.8 µm bands than HR6 family (red spectrum), even a wider hydroxylation band. The Half Width Half Maximum (HWHM), i.e. the width of band between the band center and the half height of the isolated band is 0.061 for the LR3 family and 0.05 for the HR6 family.

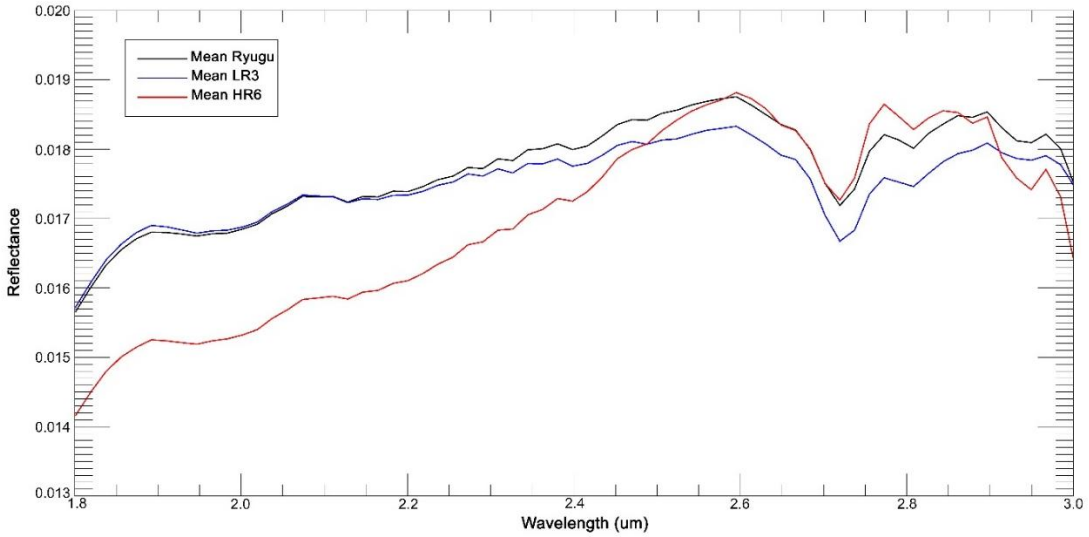

Figure 10: Mean spectrum of Ryugu (black) compared with the mean spectrum of LR3 family (blue spectrum) and HR6 family (red spectrum).

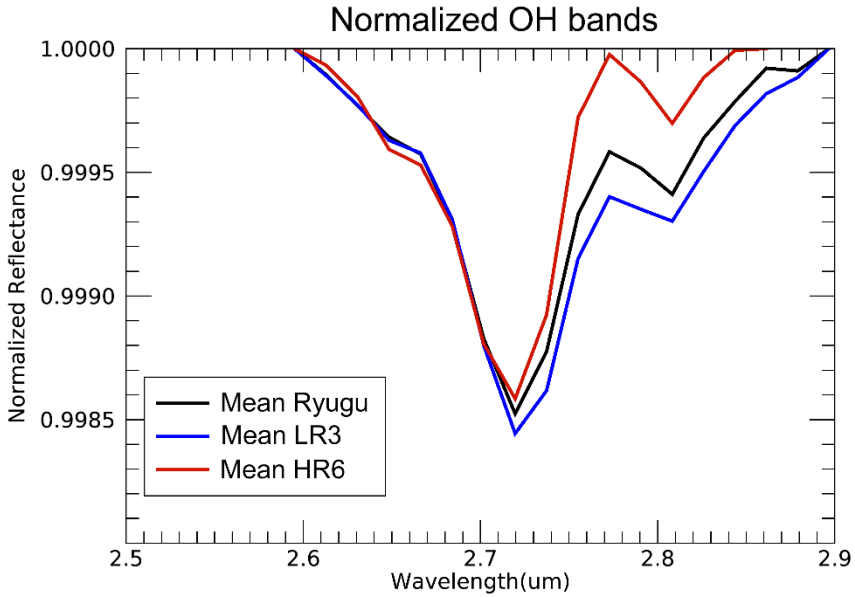

Figure 11: Isolated and normalized hydroxylation bands (2.7 and 2.8 µm band) for the LR3 family (blue spectrum), HR6 family (red spectrum) and mean Ryugu (black spectrum).

6. Geomorphological distribution of the slope families

We combined the distribution of each slope family with the Ryugu geological map (produced in *Sugita et al., 2019*) in order to associate the spectral variations to geomorphological features. We

present here the distribution of the LR2, LR3, HR2, HR3, HR4, HR5 and HR6 family, which are satisfactory to identify the trend.

In ***Figure 12, Image A***, the LR2 family is superimposed on the Ryugu geological map, noting that the family is mainly located on the equatorial ridge and in the northern hemisphere. This family is almost totally coincident with the topographic highs observed in *Morota et al. (2020)*. Spectra belonging to LR2 family are coincident to quasi-circular depressions at higher latitudes and to the rims of both smaller and larger impact craters, such as Urashima Crater, Kintaro Crater, Brabo Crater, Kolobok Crater, and a crater at 30°N; 150°E.

The LR3 family, ***Figure 12, Image B*** corresponds to the topographic highs *(Morota et al., 2020)* in the northern hemisphere.

Inversely to the LR families, which are mainly located in the northern hemisphere, the HR families characterizes the southern hemisphere.

In ***Figure 13, Images A, B, C, D,*** the distribution of HR2, HR3, HR4 and HR5 families are shown on Ryugu geological map, respectively. We can notice that these families are mainly located on the walls and floors of craters, in addition to areas around Otohime Saxum and Ejiima Saxum. Spectra with increasing spectral slope, i.e. moving from the HR2 family to the HR5 family, are progressively coincident with inner areas of craters. In particular, the HR4 family (***Figure 13, Image C***) represents the deeper part of crater floor of Momotaro, Kibidango, Urashima Crater and two unnamed impact craters (one located at 20°S;15°E and the other crater at about 30°S; 345°E). Even the east side of Ejima Saxum and the north area of Otohime Saxum are also part of the HR4 family.

Then, the deepest part of Momotaro crater and of the unnamed impact crater located at about 30°S, 345°E belong to HR5 family, in addition to Ejima and Otohime Saxum and a group of boulders (identified by the geological map) in the northern hemisphere.

In particular, the central part of Ejima Saxum (observed in the bottom part of ***Figure 14***) is characterized by the reddest spectral slope, since it belongs to the HR6 family (***Figure 13, Image E***), in addition to the unnamed region made of large boulders in the northern hemisphere.

The LR families, characterized by a bluer NIRS3 spectral slope and a NIR brightening, are mainly located in the equatorial ridge and in the northern hemisphere, and most of the areas are coincident with the regions with a bluer VIS slope, estimated by using the ONC data *(Sugita et al., 2019)*.

The HR families show a redder NIRS3 slope and a NIR spectral darkening, and, as well as the areas with a redder VIS slope and VIS darkening *(Sugita et al., 2019)*, they are mostly in the floors of craters.

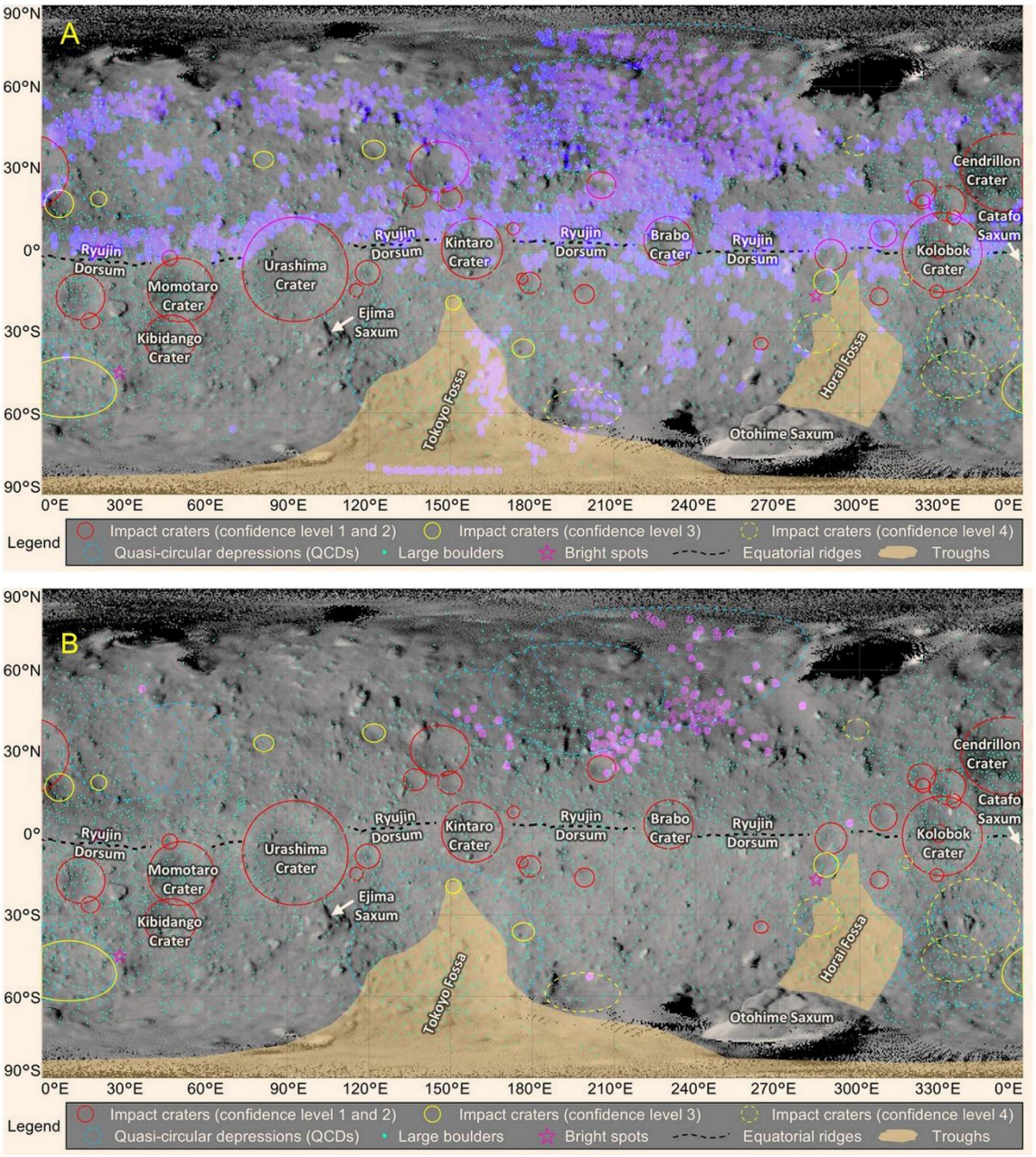

Figure 12: A) Distribution of LR2 family and B) distribution of LR3 family superimposed on the geological map of Ryugu. The LR2 family is mainly distributed in the northern hemisphere, on equatorial ridge and in rims of craters, which are topographic highs. The LR3 family is coincident with the topographic highs in northern hemisphere.

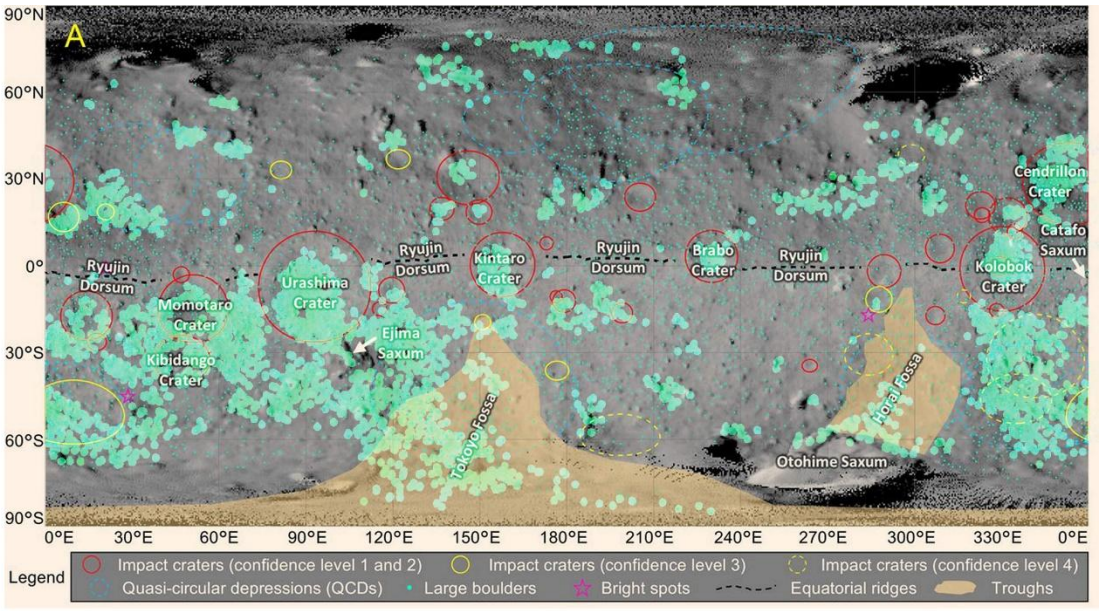
A
90°N
60°N
30°N
0°
30°S
60°S
90°S
0°E 30°E 60°E 90°E 120°E 150°E 180°E 210°E 240°E 270°E 300°E 330°E 0°E
Ryujin Dorsum
Momotaro Crater
Kibidango Crater
Urashima Crater
Ejima Saxum
Kintaro Crater
Brabo Crater
Cendrillon Crater
Catafo Saxum
Kolobok Crater
Horai Fossa
Tokoyo Fossa
Otohime Saxum
Legend
Impact craters (confidence level 1 and 2)
Impact craters (confidence level 3)
Impact craters (confidence level 4)
Quasi-circular depressions (QCDs)
Large boulders
Bright spots
Equatorial ridges
Troughs

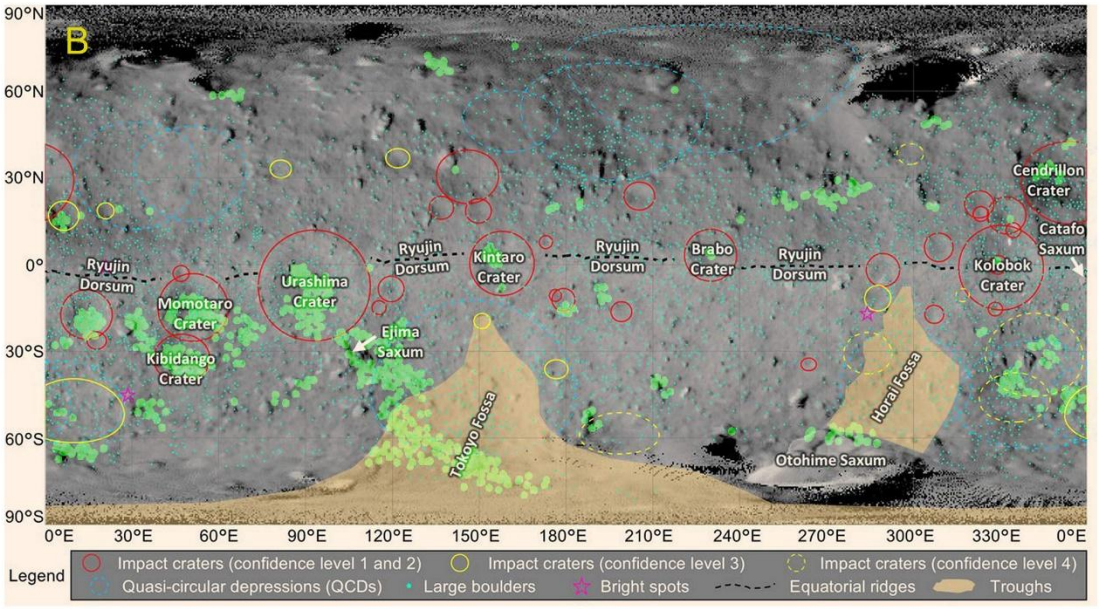
B
90°N
60°N
30°N
0°
30°S
60°S
90°S
0°E 30°E 60°E 90°E 120°E 150°E 180°E 210°E 240°E 270°E 300°E 330°E 0°E
Ryujin Dorsum
Momotaro Crater
Kibidango Crater
Urashima Crater
Ejima Saxum
Kintaro Crater
Brabo Crater
Cendrillon Crater
Catafo Saxum
Kolobok Crater
Horai Fossa
Tokoyo Fossa
Otohime Saxum
Legend
Impact craters (confidence level 1 and 2)
Impact craters (confidence level 3)
Impact craters (confidence level 4)
Quasi-circular depressions (QCDs)
Large boulders
Bright spots
Equatorial ridges
Troughs

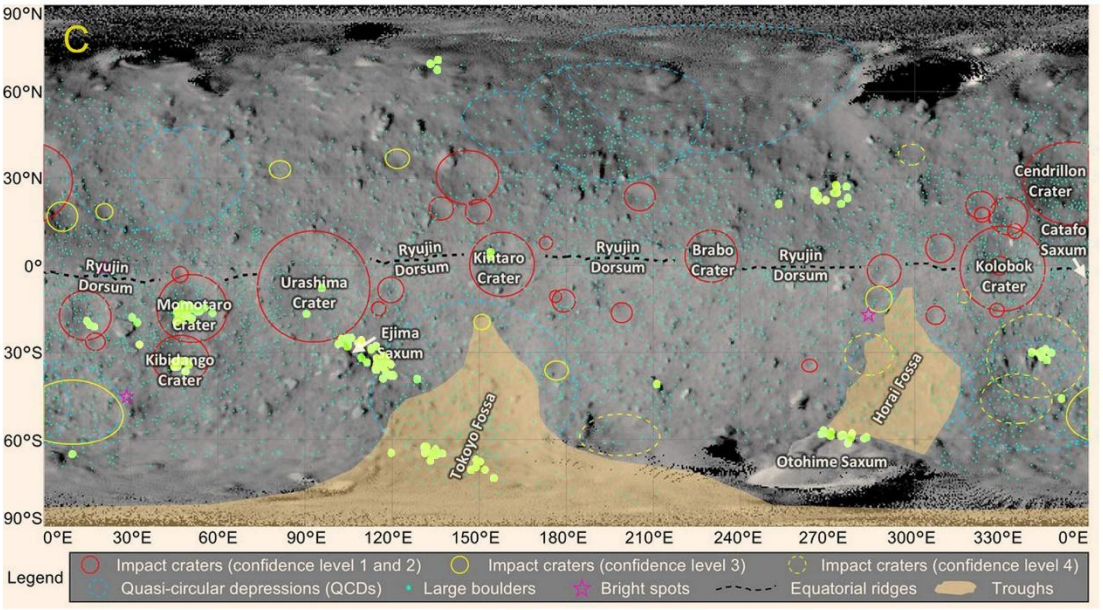
C
90°N
60°N
30°N
0°
30°S
60°S
90°S
0°E 30°E 60°E 90°E 120°E 150°E 180°E 210°E 240°E 270°E 300°E 330°E 0°E
Ryujin Dorsum
Momotaro Crater
Kibidango Crater
Urashima Crater
Ejima Saxum
Kintaro Crater
Brabo Crater
Cendrillon Crater
Catafo Saxum
Kolobok Crater
Horai Fossa
Tokoyo Fossa
Otohime Saxum
Legend
Impact craters (confidence level 1 and 2)
Impact craters (confidence level 3)
Impact craters (confidence level 4)
Quasi-circular depressions (QCDs)
Large boulders
Bright spots
Equatorial ridges
Troughs

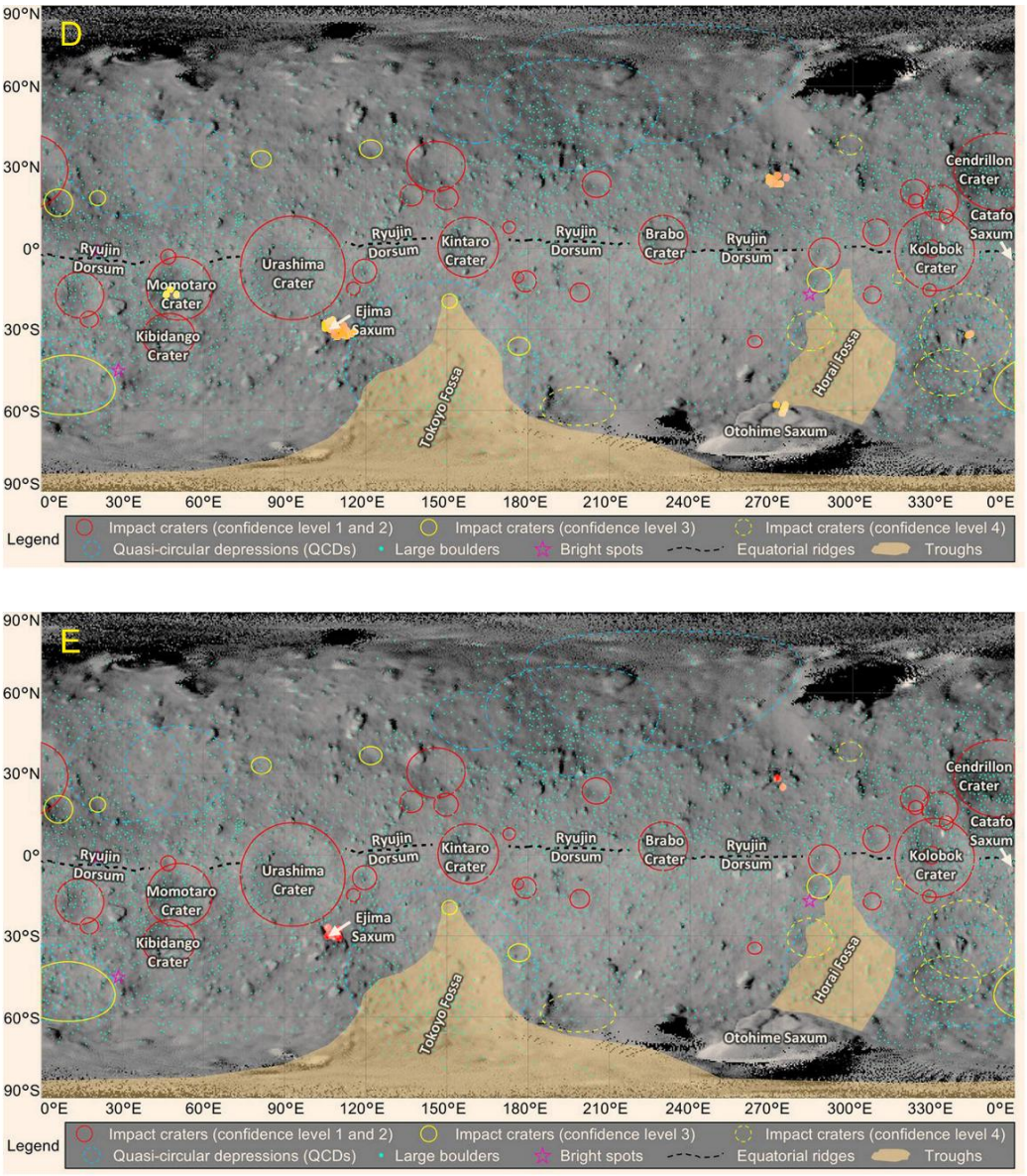

Figure 13: Distribution of HR families superimposed on the geological map of Ryugu. A) The HR2 family is in the southern hemisphere and coincident with crater walls and crater floors. B) The HR3 family is coincident with inner part of crater floors, in addition to the northern area of Otohime Saxum and to areas surrounding Ejima Saxum. C) The HR4 family is mainly localized in deeper part of craters, on the eastern part of Ejima Saxum and on the northern part of Otohime Saxum. D) The HR5 family is coincident with the inner part of Momotaro crater, of the unnamed crater at 30°S-345°E, on Ejima and Otohime Saxa and a group of boulders in the northern hemisphere. E) The HR6 family involves the central part of Ejima Saxum and unnamed boulders in the northern hemisphere.

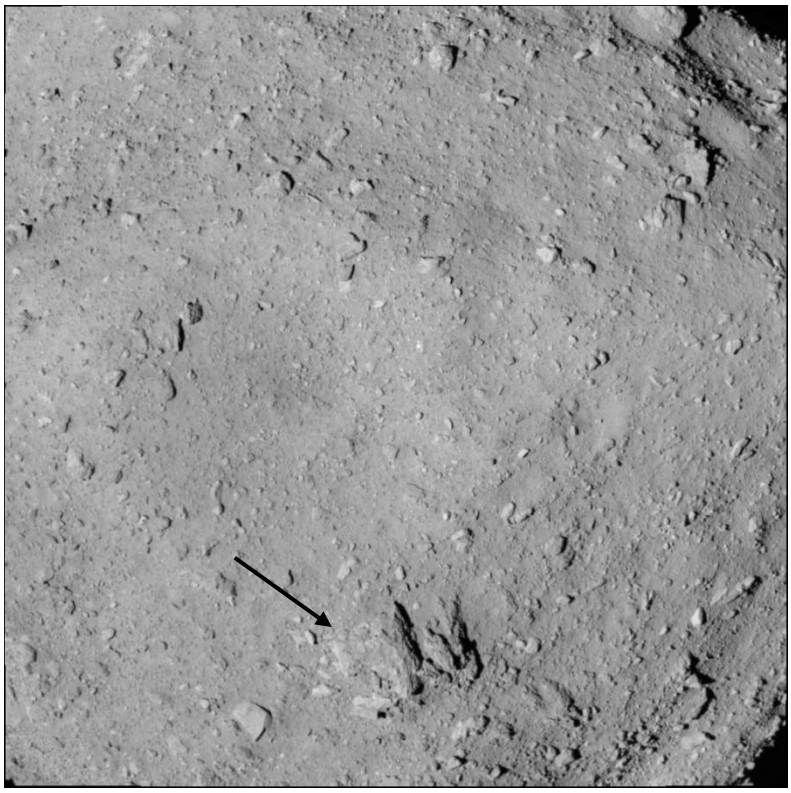

Figure 14: ONC image of Ryugu (hyb2_onc_20180801_160557_tvf_l2c), where the Ejima Saxum can be observed in the bottom part of the image, marked by a black arrow.

7. Discussion

The analysis of Ryugu spectral slope allowed us to define two slope families: families with a more positive spectral slope than the mean slope and indicated as High-Red-Sloped families (HR) and families with spectral slope values lower than the mean slope and termed as Low-Red-Sloped families (LR).

The spectral and geomorphological analysis of these families produced the following results.

- The HR families are areas with increasing spectral slope, and the spectral reddening is related to spectral darkening, weakening and narrowing of OH bands; the HR families are in the southern hemisphere and are coincident with floors and walls of impact craters, as well as with Ejima and Otohime Saxum; the areas with the most positive spectral slope is the HR6 family, corresponding to Ejima Saxum.

- The LR families are areas with a flattening in the spectral slope, in addition to a deepening and widening of OH bands and a uniform reflectance value (almost coincident with the spectral slope of Mean Ryugu); the LR families are in the northern hemisphere and on the equatorial ridge, and are coincident with the rims of impact craters. The areas with the most spectral flattening belong to the LR3 family and are coincident with the topographic highs in the northern hemisphere.

Small bodies which are not protected by atmosphere or magnetic field, as Ryugu, are constantly exposed to space weathering processes, such as micro-meteoritic bombardment and solar wind irradiation. These mechanisms, in addition to thermal metamorphism experienced by Ryugu *(Watanabe et al., 2019)*, could induce variations in the spectral properties of the surface materials and could be responsible of the observed spectral variations. The effects of space weathering and thermal metamorphism on asteroids are simulated in laboratory by irradiating meteorites and/or minerals with laser and ion (to simulate the micro-meteoritic bombardment and the solar wind, respectively) or by undergoing samples to heating cycles (to simulate thermal metamorphism). The reflectance spectra of processed samples could experience VIS-NIR spectral darkening/brightening and reddening/bluing *(Lantz et al., 2017)*, variation in the intensity of OH bands *(Matsuoka et al., 2015; Hanna et al., 2019)* and in the width of OH bands *(Hanna et al., 2019).*

Ryugu is a C-type asteroid, in particular a Cb-type, spectrally similar to CI and CM carbonaceous chondrites (CCs). There is no certain evidence that Ryugu started his life as a CI/CM-like object, since it is possible that Ryugu became like these CCs later. The original nature of Ryugu will be established by the in-depth analysis of the returned sample in the terrestrial laboratories. However, until that time, we explain the spectral properties of Ryugu by assuming that its actual nature is the original one, and therefore spectrally similar to the CI/CM CCs.

CCs are aqueously altered material, composed by a poorly heated matrix and (except for CIs) a high temperature fraction containing Calcium-Aluminium rich Inclusion (CAIs) *(Vernazza et al., 2013)*.

454 CM carbonaceous chondrites are aqueously altered rocks, whose products include serpentine-group
455 phyllosilicates, saponite-group phyllosilicates, tochilinite, tochilinite-serpentine intergrowths and
456 sulfates *(Zolensky and McSween, 1988)*. The matrix of CMs represent the 57-85 vol% *(McSween,*
457 *1979)*: it is a complex assemblage mainly composed of serpentine and tochilinite-serpentine
458 intergrowths, with reduced amount of magnetite, Ca-phosphates, organic matter, saponite and
459 carbonates *(Zolensky et al., 1993).* The dominant phase in the matrix is the Fe-rich serpentine group
460 phyllosilicates such as cronstedtite *(Buseck and Hua, 1993)* and the second dominant phase is the
461 intergrowth of cronstedtite/serpentine and tochilinite *(Brearley and Jones, 1998; Buseck and Hua,*
462 *1993)*. In particular, if the cronstedtite is the dominant phyllosilicate in CM matrix, the ferroan Mg-
463 serpentine is also common (Brearley and Jones, 1998). In CM chondrites, a strong negative
464 correlation occurs between the abundance of Fe-cronstedtite and Mg-serpentine, suggesting that a
465 transition from Fe-rich to Mg-rich serpentine occurs as a consequence of aqueous alteration *(Howard*
466 *et al., 2009; 2011).*
467 CI carbonaceous chondrites also experienced aqueous alteration processes, where pre-existing
468 anhydrous silicates have been almost completely transformed to phyllosilicates (50-60 vol%), with
469 intergrown ferrihydrite; oxides are present in rich abundances (mainly magnetite and maghemite), in
470 addition to carbonates, sulphides, sulfates and organic matter *(Richardson, 1978; Zolensky and*
471 *McSween, 1988; Buseck and Hua, 1993; Zolensky et al., 1993; Brearley and Jones, 1998; Gounelle*
472 *and Zolensky, 2001)*. The matrix is dominated by phyllosilicates, in particular by different proportion
473 of intergrown Fe-bearing serpentine and saponite, intimately intergrown with ferrihydrite (*McSween,*
474 *1987; Tomeoka, 1990; Brearley and Jones, 1998)*. With increasing aqueous alteration, CIs are richer
475 in serpentine and saponite *(Howard et al., 2010).*
476 The space weathering effects on C-type asteroids are not well defined, since laboratory simulations
477 on analogue CI and CM meteorites produced conflicting results.
478 Ion irradiation experiments on pressed pellet of different types of CCs meteorites linked the spectral
479 variation to initial composition/albedo *(Lantz et al., 2017):* bright CCs with an albedo greater than

480 9% (such as CV and CO, rich in chondrules and anhydrous silicates) showed a spectral reddening and
481 darkening after irradiation; dark CCs with an albedo lower than 5% (such as CI and CM, dominated
482 by matrix with organics and hydrous silicates) exhibited a spectral bluing and brightening after the
483 experiment *(Lantz et al., 2017).*
484 Pellet of powdered sample of CM2 Murchison, after being exposed to pulse laser irradiation at
485 energies of 5, 10 and 15 mJ, exhibited a spectral darkening and flattening in the Near-Infrared spectral
486 range and a suppression of the O-H stretching mode at about 2.7 μm in phyllosilicates *(Matsuoka et*
487 *al., 2015).* The sample was also laser irradiated with lower energies of 0.7, 1, 2 and 5 mJ, confirming
488 the spectral darkening and bluing/flattening at increasing laser energies, in addition to the weakening
489 of the O-H band of about 15% *(Matsuoka et al., 2020)*.
490 Laser irradiation on pressed samples of CI, CM and Tagish Lake meteorites revealed a spectral
491 darkening and bluing after irradiation (in the spectral range included between 0.3 and 2.5 μm range),
492 in addition to the suppression of the OH band at about 2.7 μm *(Hiroi et al., 2013)*.
493 Space weathering simulations have been also performed on fragments or chips of CCs, which better
494 preserve the petrographic properties of the sample and the interrelationships between mineral phases
495 *(Thompson et al., 2019)* than pressed pellet. It is likely that fragments or chips of CCs could better
496 represent the surface of Ryugu, that is rich in boulders.
497 A fragment of the C2 Tagish Lake meteorite was ion-irradiated at low energy (4 keV) with an ion
498 beam composed by He^+ and with an ion beam composed by Ar^+. The He^+ flux produced a spectral
499 reddening in the reflectance spectra of irradiated meteorite (spectral range included between 0.5 and
500 2.5 μm), whereas the Ar^+ flux generated a spectral flattening *(Vernazza et al., 2013).*
501 Ion irradiation (4 keV) on a section of CM2 Murchison meteorite produced, in the Near-Infrared
502 spectral rage, a lower reflectance value and a spectral reddening compared to the unirradiated sample,
503 in addition to a weakening and narrowing of the 2.7-μm band. The irradiation caused the
504 amorphization of phyllosilicates in the Murchison sample at a depth of 150-200 nm and inclusions of
505 nanophase iron particles (2-5 nm) were observed in the amorphized phyllosilicates *(Keller et al.,*

2015). The nanophase iron particles, in small bodies, could be the result of solar wind implantation in addition to amorphization of target material and redeposition of sputtered material *(Noguchi et al., 2011; Noguchi et al., 2014)*. Pulsed-laser experiments on chips of CM2 Murchison meteorite revealed that laser-irradiated areas are darker and bluer than unirradiated ones, for the production of nanophase iron particles *(Thompson et al., 2019)* or FeS-rich nanoparticles *(Matsuoka et al., 2015)*.

A Murchison powder samples (<63 µm) was heated for 1 week at 400 °C, 500 °C, 600 °C, 700 °C, 800 °C and 900 °C: the absorption band located at 2.7-3.0 µm gradually weakens up to 500 °C and vanishes at 600-700 °C *(Hiroi et al., 1996)* for the dehydration/dehydroxylation and transformation of phyllosilicates to olivine and pyroxene *(Zolensky et al., 1994).* Furthermore, a spectral bluing occurs in the NIR spectral range (1.5-2.5 µm) at higher heating temperatures *(Hiroi et al., 1996; Cloutis et al., 2019)*; a spectral darkening is observed at higher temperatures up to 600 °C, then a brightening occurs *(Hiroi et al., 1996)*.

The heating experiment on CM-like material showed that the 2.7-µm band, related to OH in phyllosilicates, becomes sharper before disappearing by 800°C *(Hanna et al., 2019).*

In ***Table 3*** the effects of space weathering simulation are summarized for CM2 Murchison sample and CM-like material, given the spectral similarities between Ryugu and the CM carbonaceous chondrites *(Kitazato et al., 2019)*.

Granulometry can also alter spectral properties of the surface. The Murchison meteorite was sieved, and different samples were obtained with the maximum particle sizes of 1000, 500, 250, 150, 90 and 45 µm *(Cloutis et al., 2018).* At decreasing maximum grain size, the spectra become brighter and more red-sloped in the 0.6-1.8 µm spectral range *(Cloutis et al., 2018)*. In a powdered mixture with increasing fine-sized particles, the reflectance spectra become redder and brighter and absorption bands generally decrease *(Cloutis et al., 2018).* Furthermore, a mixture with fine grains of opaque phase not intimately mixed is characterized by a spectral reddening *(Cloutis et al., 2011).*

Table 3: Effects of space weathering simulation on CM2 Murchison and CM-like material, the CCs spectrally similar to Ryugu. For each experiment (ion irradiation, laser irradiation and heating procedure), the variation in reflectance, spectral slope and OH-bands are reported. In particular, the columns represent: the experiment, the sample on which the experiment was performed, the spectral variations due to the experiment, the references of the experiment and the slope families that are supposed to have experienced the corresponding alteration. The increasing of reflectance, spectral slope (reddening), as well as the deepening and widening of OH-band is represented by the "+" symbol, whereas the lowering of reflectance, spectral slope (bluing or flattening), in addition to the weakening and narrowing of OH band is characterized by the "–" symbol. References for the experiments: [a], Keller et al. (2019); [b], Thompson et al. (2019); [c] Matsuoka et al. (2015); [d] Hiroi et al. (1996); [e] Hannah et al. (2019).

Experiment	**Sample**	**Space Weathering Effects**				**References**	**Slope families**
		Reflectance	**Slope**	**Intensity of OH-band**	**Width of OH-band**		
Ion Irradiation	*CM2 Murchison*	–	+	–	–	[a]	LR1; LR2; LR3; HR1; HR2; HR3; HR4; HR5; HR6
Laser irradiation	*CM2 Murchison*	–	–	–		[b, c]	HR2; HR3; HR4; HR5
Heating	*CM2 Murchison*	– (up to 600°C) + (600-900°C)	–	–		[d]	LR1; LR2; LR3; HR1; HR2; HR3; HR4; HR5; HR6
	CM-like material				–	[e]	

To explain the spectral variations observed on Ryugu surface, three processes need to be taken into account: 1) the thermal metamorphism experienced by the material composing Ryugu for the fragmentation of parent body; 2) the impacts on the surface during the permanence of Ryugu in the Main-Belt, which produced larger craters; 3) the solar wind irradiation on the surface during both the

permanence in the Main Belt and in its actual permanence in the Near-Earth orbit, lasting at least from 8 Myr.

Ryugu shows weak hydroxylation bands in the 2.7-2.8 μm range, suggesting that its surface is poor in OH-bearing minerals. Likely, the thermal metamorphism experienced as a consequence of parent body's fragmentation *(Watanabe et al., 2019)* heated the material that now compose Ryugu up to 400-500 °C, producing weak OH bands and an overall spectral darkening and bluing, as observed in *Hiroi et al. (1996)*. Furthermore, the solar wind irradiation could have led to a spectral reddening, in addition to a decreasing in the reflectance and in the intensity of the OH bands, as observed in the laboratory experiments with ion irradiation *(Keller et al., 2015)*. The solar wind acted on Ryugu surface in the Main Belt and it is still active in its current Near-Earth orbit. In particular, the flux density of solar wind at about 3 AU (corresponding to a region of Main Belt) has been estimated to be about $1.5 \cdot 10^{7} cm^{-2} s^{-1}$ *(Brunetto et al., 2014)*, whereas the flux at 1 AU (almost coincident with the semi-major axis of Ryugu) is about $3 \cdot 10^{8} cm^{-2} s^{-1}$ *(Schwenn, 2005)*. The effects of thermal metamorphism and solar irradiation could explain the spectral properties of the mean surface of Ryugu and the family close to it, i.e. HR1, LR1 and LR2 families, characterized by mean values of both OH-bands intensity, moderate spectral darkening and reddening. The LR2 and LR3 family correspond to topographic highs *(Sugita et al., 2019)*, which probably exposed fresher materials that experienced less dehydroxylation. The LR3 family is coincident with the topographic highs in the northern hemisphere and it is the family with the deepest 2.7- and 2.8- μm bands and with the flattest and brightest spectra: the LR3 family could represent a more hydroxylated and less altered area.

The interior part of craters is more red-sloped and darker than HR1, LR1 and LR2 families, with weaker and narrower OH bands: it is likely that in these geological features, corresponding to the families from HR2 to HR5, the effects of impacts and solar wind irradiation overlap, in addition to the previous thermal metamorphism. The impacts generating craters likely produced a darkening and spectral flattening of the thermally altered surface, as observed in the laboratory experiment

572 *(Thompson et al., 2019)*; in addition, the impact process could have fragmented larger grains and
573 produced finer regoliths, which could yield a spectral reddening and a brightening, as noted by *Cloutis*
574 *et al. (2018)*. These two effects could be masked and/or enhanced by the spectral variations induced
575 by the solar wind irradiation. Therefore, the solar flux could contribute, from the formation of Ryugu
576 as today, to a further spectral reddening and darkening of the Ryugu's thermally altered and cratered
577 surface, in addition to a weakening and narrowing of OH bands, as the ion irradiation experiments
578 demonstrated *(Keller et al., 2015)*.

579 The HR6 family, coincident with Ejima Saxum, is the family with the highest spectral slope, with the
580 lowest value in reflectance and with the weakest OH bands. The spectral properties of this family
581 could be explained by the combination of the thermal processes and ion irradiation. As previously
582 described (*Hiroi et al., 1996; Keller et al., 2015)*, the thermal heating experienced by Ryugu likely
583 produced an initial spectral bluing, in addition to a spectral darkening and a OH-band weakening,
584 whereas the subsequent and constant solar wind irradiation could be responsible of the spectral
585 reddening currently observable, with an additional darkening and OH weakening. Ejima Saxum is a
586 dark and rugged boulder, partially buried by asymmetrical distributed fragmental debris deposits, i.e.
587 regolith *(Sugita et al., 2019)*. It is possible that the regolith covering the boulder, characterized by
588 finer size of grains with respect to the boulder itself, is responsible of the strong reddening of this
589 area (the HR6 family), as noted in laboratory experiments *(Cloutis et al., 2011; Cloutis et al., 2019)*.

590

591 ## 8. Conclusion

592 By studying the variability of NIRS3 spectral slope on Ryugu surface, we defined 9 "slope families",
593 characterized by a progressive spectral reddening and darkening, a weakening and narrowing OH
594 bands. The spectral variability in slope, reflectance and absorption bands is a consequence of the
595 thermal metamorphism experienced by Ryugu after the catastrophic disruption of its parent body and

space weathering processes occurred (as impact cratering) and occurring (solar wind irradiation) on its surface.

We suggest that the HR1, LR1 and LR2 families are fresher material on Ryugu's surface, which, along with the LR3 family, experienced minor alteration and OH devolatilization (due to thermal metamorphism and solar wind irradiation); the HR2, HR3, HR4, HR5 families are the most altered areas, given that they are the result of three processes (thermal metamorphism, impact cratering and solar wind irradiation). The HR6 family is coincident with Ejima Saxum: this family experienced a space weathering process like that of fresher families (thermal metamorphism and solar wind irradiation) but the strong spectral reddening and darkening is likely due to the fine-sized material covering the large boulder.

Acknowledgments

The Hayabusa2 spacecraft was developed and built under the leadership of Japan Aerospace Exploration Agency (JAXA), with contributions from the German Aerospace Center (DLR) and the Centre National d'Études Spatiales (CNES), and in collaboration with NASA, Nagoya University, University of Tokyo, National Astronomical Observatory of Japan (NAOJ), University of Aizu, Kobe University, and other universities, institutes, and companies in Japan. We also thank the engineers who contributed to the success of Hayabusa2 operations.

This work is founded by the Italian Space Agency (ASI), which has been developed under the agreement 2018-27-HH-0.

References

620 Adams J. B., 1974, *Visible and near-infrared diffuse reflectance spectra of pyroxenes as applied to*
621 *remote sensing of solid objects in the solar system*, Journal of Geophysical Research **79**, 4829–
622 4836, https://doi.org/10.1029/JB079i032p04829.
623 Arai, T. et al., 2017, *Thermal Imaging Performance of TIR Onboard the Hayabusa2 Spacecraft*,
624 Space Science Reviews **208**, 239-254, doi: 10.1007/s11214-017-0353-9.
625 Bottke, W. F. et al., 2015, *In search of the source of asteroid (101955) Bennu: Applications of the*
626 *stochastic YORP model*, Icarus **247**, 191–217, doi:10.1016/j.icarus.2014.09.046.
627 Brearley, A.J. and Jones, R.H., 1998, *Chondritic meteorites*, In: Planetary Materials. In: Papike, J.J.
628 (Ed.), Reviews in Mineralogy **36**, Mineralogical Society of America, Washington, DC (Chapter
629 3).
630 Brunetto, R. et al., 2014, *Ion irradiation of Allende meteorite probed by visible, IR, and Raman*
631 *spectroscopy*, Icarus **237**, 278-292, http://dx.doi.org/10.1016/j.icarus.2014.04.047.
632 Buseck, P.R. and Hua, X., 1993, *Matrices of carbonaceous chondrite meteorites*, Annual Review of
633 Earth and Planetary Science **21**, 255–305,
634 https://www.annualreviews.org/doi/pdf/10.1146/annurev.ea.21.050193.001351.
635 Clark, R.N. and Roush, T.L., 1984, *Reflectance spectroscopy: quantitative analysis techniques for*
636 *remote sensing applications*, Journal of Geophysical Research **89**, Nr. B7, 6329-6340,
637 doi:10.1029/JB089iB07p06329.
638 Clark R. N, 1999, *Chapter 1: Spectroscopy of rocks and minerals, and principles of spectroscopy*. In
639 Manual of remote sensing, volume 3, remote sensing for the Earth sciences, edited by Rencz A.
640 N. New York: John Wiley and Sons. pp. 3–58.
641 Clark R. N. et al., 2007, USGS digital spectral library splib06a, Data Series, 231, U.S. Geological
642 Survey, Reston, VA, http://speclab.cr.usgs.gov/spectral.lib06.
643 Cloutis, E. A. et al., 2011, *Spectral reflectance properties of carbonaceous chondrites: 1. CI*
644 *chondrites*, Icarus **212**, 180-209, doi: 10.1016/j.icarus.2010.12.009.

645 Cloutis, E. A. et al., 2018, *Spectral reflectance "deconstruction" of the Murchison CM2*
646 *carbonaceous chondrite and implications for spectroscopic investigations of dark asteroids*, Icarus
647 **305**, 203-224, https://doi.org/10.1016/j.icarus.2018.01.015.
648 Cloutis, E. A. et al., 2019, *Redder/bluer, brighter/darker, deeper/shallower absorption bands: effects*
649 *of physical properties, space weathering, and observing geometry on reflectance spectra of the*
650 *Murchison CM2 carbonaceous chondrite*, Asteroid Science in the Age of Hayabusa2 and OSIRIS-
651 REx, 5-7 November 2019, University of Arizona in Tucson, AZ, Abstract #2040.
652 Galiano, A. et al., 2018, *Continuum definition for ~3.1. ~3.4 and ~4.0 μm absorption bands in Ceres*
653 *spectra and evaluation of effects of smoothing procedure in the retrieved spectral parameters*,
654 Advances in Space Research **62**, Issue 8, 2342-2354, https://doi.org/10.1016/j.asr.2017.10.039.
655 Galiano, A. et al., 2019, *Spectral analysis of the Cerean geological unit crater central peak material*
656 *as an indicator of subsurface mineral composition*, Icarus **318**, 75-98,
657 https://doi.org/10.1016/j.icarus.2018.05.020.
658 Gounelle, M. and Zolensky, M.E., 2001, A terrestrial origin for sulfate veins in CI1 chondrites,
659 Meteoritics & Planetary Science **36**, 1321–1329, https://doi.org/10.1111/j.1945-
660 5100.2001.tb01827.x.
661 Hanna, R.D. et al., 2019, *What is the hydrated phase on Bennu's surface?,* Asteroid Science in the
662 Age of Hayabusa2 and OSIRIS-REx, 5-7 November 2019, University of Arizona in Tucson, AZ,
663 Abstract #2029.
664 Hirabayashi, M. et al., 2019, *Spin-driven evolution of top-shaped asteroids at fast and slow spins seen*
665 *from (101955) Bennu and (162173) Ryugu*, Asteroid Science in the Age of Hayabusa2 and
666 OSIRIS-REx, 5-7 November 2019, University of Arizona in Tucson, AZ, Abstract #2047.
667 Hiroi, T. et al., 1996, *Thermal metamorphism of the C, G, B, and F asteroids seen from the 0.7 μm,*
668 *3 μm, and UV absorptions strengths in comparison with carbonaceous chondrites*, Meteoritics
669 and Planetary Science **31**, 321-327.

Hiroi, T. et al., 2013, *Keys to detect space weathering on Vesta: changes of Visible and Near-Infrared reflectance spectra of HEDs and carbonaceous chondrites*, 44th Lunar and Planetary Science Conference, abstract #1276.

Howard K. T. et al., 2009, *Modal mineralogy of CM2 chondrites by X-ray diffraction (PSD-XRD), Part 1: Total phyllosilicate abundance and the degree of aqueous alteration*, Geochimica et Cosmochimica Acta **73**, 4576–4589, doi: 10.1016/j.gca.2009.04.038.

Howard, K. T. et al., 2010, *Aqueous alteration, ''serpentinization'' and the CM-C2ung-CI connection by PSD-XRD*, 73rd Annual Meeting of the Meteoritical Society, Abstract #5186.

Howard K. T. et al., 2011, *Modal mineralogy of CM chondrites by X-ray diffraction (PSD-XRD): Part 2. Degree, nature and settings of aqueous alteration*, Geochimica et Cosmochimica Acta **75**, Issue 10 2735–2751, doi:10.1016/j.gca.2011.02.021.

Iwata, T. et al., 2017, *NIRS3: The Near Infrared Spectrometer on Hayabusa2*, Space Science Reviews **208**, 317-337, doi: 10.1007/s11214-017-0341-0.

Kameda, S. et al., 2017, *Preflight Calibration Test Results for Optical Navigation Camera Telescope (ONC-T) Onboard the Hayabusa2 Spacecraft*, Space Science Reviews **208**, 17-31, doi: 10.1007/s11214-015-0227-y.

Keller, L. P. et al., 2015, *Ion irradiation experiments on the Murchison CM2 carbonaceous chondrite: simulating space weathering of primitive asteroids*, Lunar and Planetary Science Conference, https://ntrs.nasa.gov/search.jsp?R=20150001922 2020-02-07T15:07:50+00:00Z.

Kitazato, K. et al., 2109, *The surface composition of asteroid 162173 Ryugu from Hayabusa2 near-infrared spectroscopy*, Science **364**, Issue 6437, 272-275, doi: 10.1126/science.aav7432.

Lantz, C. et al., 2017, *Ion irradiation of carbonaceous chondrites: A new view of space weathering on primitive asteroids*, Icarus **285**, 43-57, http://dx.doi.org/10.1016/j.icarus.2016.12.019.

Longobardo, A. et al., 2014, *Photometric behaviour of spectral parameters in Vesta dark and bright regions as inferred by the Dawn VIR spectrometer*, Icarus **240**, 20-35, doi: 10.1016/j.icarus.2014.02.014.

696 Longobardo, A. et al., 2019a, *Mineralogy of the Urvara-Yalode region on Ceres*, Icarus **318**, 241-
697 250, doi: 10.1016/j.icarus.2017.12.011.
698 Longobardo, A. et al., 2019b, *Photometry of Ceres and Occator faculae as inferred from VIR/Dawn*
699 *data*, Icarus **320**, 97-109, doi: 10.1016/j.icarus.2018.02.022.
700 Matsuoka, M. et al., 2015, *Pulse-laser irradiation experiments of Murchison CM2 chondrite for*
701 *reproducing space weathering on C-type asteroids*, Icarus **254**, 135-143,
702 http://dx.doi.org/10.1016/j.icarus.2015.02.029.
703 Matsuoka, M. et al., 2020, *Space weathering simulations with low-energy laser irradiation of*
704 *Murchison CM chondrite for reproducing micrometeoroid bombardments on C-type asteroids*,
705 The Astrophysical Journal Letters **890**, Issue 2, id.L23, (12pp), doi: 10.3847/2041-8213/ab72a4.
706 McSween Jr., H.Y., 1979, *Alteration in CM carbonaceous chondrites inferred from modal and*
707 *chemical variations in matrix*, Geochimica et Cosmochimica Acta **43**, Issue 11, 1761-1770,
708 https://doi.org/10.1016/0016-7037(79)90024-3.
709 McSween Jr., H.Y., 1987, *Aqueous alteration in carbonaceous chondrites: Mass balance constraints*
710 *on matrix mineralogy*, Geochimica et Cosmochimica Acta **51**, Issue 9, 2469–2477,
711 https://doi.org/10.1016/0016-7037(87)90298-5.
712 Michel, P. et al., 2001, *Collisions and gravitational reaccumulation: forming asteroid families and*
713 *satellites*, Science **294**, Issue 5547, 1696-1700, doi: 10.1126/science.1065189.
714 Mizuno, T. et al., 2017, *Development of the Laser Altimeter (LIDAR) for Hayabusa2*, Space Science
715 Reviews **208**, 33-47, doi: 10.1007/s11214-015-0231-2.
716 Morota, T. et al., 2020, *Sample collection from asteroid (162163) Ryugu by Hayabusa2: Implications*
717 *for surface evolution*, Science **368**, 654-659, doi: 10.1126/science.aaz6306.
718 Noguchi, T. et al., 2011, *Incipient space weathering observed on the surface of Itokawa dust particles*,
719 Science **333**, Issue 6046, 1121-1125, doi: 10.1126/science.1207794.
720 Noguchi, T. et al., 2014, *Space weathered rims found on the surfaces of the Itokawa dust particles*,
721 Meteoritics & Planetary Science **49**, Issue 2, 188-214, https://doi.org/10.1111/maps.12111.

722 Palomba, E. et al., *Detection of new olivine-rich locations on Vesta*, Icarus **258**, 120-134, doi:
723 10.1016/j.icarus.2015.06.011.
724 Richardson, S.M., 1978, *Vein formation in the C1 carbonaceous chondrites*, Meteoritics **13**, 141–
725 159, doi: 10.1111/j.1945-5100.1978.tb00803.x.
726 Saiki, T. et al., 2013, *Small carry-on impactor of Hayabusa2 mission*, Acta Astronauta **84**, 227-236,
727 http://dx.doi.org/10.1016/j.actaastro.2012.11.010.
728 Schwenn, R., 2005, *Solar wind: Global properties*, Encyclopedia of Astronomy and Astrophysics (P.
729 Murdin), doi: 10.1888/0333750888/2301.
730 Sugita, S. et al., 2019, *The geomorphology, color, and thermal properties of Ryugu: Implications for*
731 *parent-body processes*, Science **364**, Issue 6437, 252-252, doi: 10.1126/science.aaw0422.
732 Tachibana, S. et al., 2017, *Initial analysis and curation plans for Hayabusa2 samples from C-type*
733 *near-Earth asteroid Ryugu will be presented*, 48th LPSC, Abstract #1850.
734 Takaki, N. et al., 2019, *Resurfacing process on Ryugu constrained by crater distribution*, Asteroid
735 Science in the Age of Hayabusa2 and OSIRIS-REx, 5-7 November 2019, University of Arizona
736 in Tucson, AZ, Abstract #2077.
737 Tardivel, S. et al., 2018, *Equatorial cavities on asteroids, an evidence of fission events*, Icarus **304**,
738 192–208, doi:10.1016/j.icarus.2017.06.03.
739 Thompson, M.S. et al., 2019, *The effects of space weathering on the organic and inorganic*
740 *components of a carbonaceous chondrite: implications for returned samples from hayabusa2 and*
741 *OSIRIS-REx*, Asteroid Science in the Age of Hayabusa2 and OSIRIS-REx, Abstract #2103.
742 Tomeoka, K., 1990, *Matrix compositions and mineralogy of Alais and Ivuna CI carbonaceous*
743 *chondrites*, 21st LPSC, 1256–1257 (abstract).
744 Tosi, F. et al., 2018, *Mineralogy and temperature of crater Haulani on Ceres*, Meteoritics & Planetary
745 Scince **53**, Nr. 9, 1902-1924, doi:10.1111/maps.13078.
746 Vernazza, P. et al., 2013, *Paucity of Tagish Lake-like parent bodies in the Asteroid Belt and among*
747 *Jupiter Trojans*, Icarus **225**, 517-525, https://doi.org/10.1016/j.icarus.2013.04.019.

748 Watanabe, S. et al., 2017, *Hayabusa2 Mission Overview*, Space Science Reviews **208**, Issue 1-4, 3-
749 16, doi:10.1007/s11214-017-0377-1.
750 Watanabe, S. et al., 2019, *Hayabusa2 arrives at the carbonaceous asteroid 162173 Ryugu- A spinning*
751 *top-shaped rubble pile*, Science **364**, Issue 6437, 268-272, doi: 10.1126/science.aav8032.
752 Zolensky, M. E. and McSween H. Y., JR., 1988, *Aqueous Alteration*, In Meteorites and the Early
753 Solar System (ed. J. F. Kerridge and M. S. Matthews), 114-143. Univ. Arizona Press.
754 Zolensky, M., Barrett, R. and Browning, L., 1993, *Mineralogy and composition of matrix and*
755 *chondrule rims in carbonaceous chondrites*, Geochim. Cosmochim. Acta **57**, Issue 13, 3123–3148,
756 https://doi.org/10.1016/0016-7037(93)90298-B.
757 Zolensky, M. E., Lipschutz, M. E. and Hiroi, T., 1994, *Mineralogy of artificially heated carbonaceous*
758 *chondrites*, 25th LPSC, Abstract #1567.
759
760
761
762